Journal Pre-proof

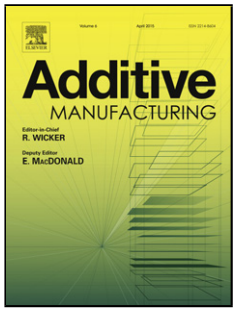

Comparison of residual stresses obtained by the crack compliance method for parts produced by different metal additive manufacturing techniques and after friction stir processing

Lv Zhao, Juan Guillermo Santos Macías, Adrien Dolimont, Aude Simar, Edouard Rivière-Lorphèvre

PII: S2214-8604(20)30871-X

DOI: https://doi.org/10.1016/j.addma.2020.101499

Reference: ADDMA 101499

To appear in: *Additive Manufacturing*

Received Date: 28 February 2020

Revised Date: 23 July 2020

Accepted Date: 27 July 2020

Please cite this article as: { doi: https://doi.org/

Comparison of residual stresses obtained by the crack compliance method for parts produced by different metal additive manufacturing techniques and after friction stir processing

Lv Zhao[a,b,d,*], Juan Guillermo Santos Macías[b], Adrien Dolimont[c], Aude Simar[b], Edouard Rivière-Lorphèvre[c]

[a]*Department of Mechanics, Huazhong University of Science and Technology, Wuhan, China*
[b]*Institute of Mechanics, Materials and Civil Engineering, UCLouvain, Louvain-la-Neuve, Belgium*
[c]*Machine Design and Production Engineering Unit, Faculty of Engineering, University of Mons, Mons, Belgium*
[d]*Hubei Key Laboratory of Engineering Structural Analysis and Safety Assessment, Wuhan, China*

Abstract

Metal additive manufacturing (AM) techniques are promising to build complex components in automotive, aerospace and biomedical industries. However, as built AM parts generally present residual stresses which may degrade the fatigue resistance of the material. Although the AM techniques have been substantially studied, few data about the residual stress level and distribution are available in literature. This paper presents residual stress measurements and analysis on the metal powder bed AM parts using the crack compliance method. Both electron beam melting (EBM) and selective laser melting (SLM) processes are investigated for two manufactured alloys, i.e., Ti6Al4V and AlSi10Mg. It is found that: (i) the EBM process results in negligible residual stresses; (ii) the SLM leads to compressive stresses in the middle, accompanied by tensile stresses at the bottom and the top of the built part; (iii) preheating the build platform in the SLM process significantly reduces the residual stresses and effectively mitigates the porosity. Moreover, we show that post-treatment by friction stir processing inverts the residual stress distribution compared to the SLM process while significantly reducing the porosity.

Keywords: Residual stresses, electron beam melting, selective laser melting, crack compliance method, friction stir processing

1. Introduction

Metal powder bed additive manufacturing (AM) offers the possibility of building complex geometry structural components which cannot be achieved by conventional machining methods.

*corresponding author: lvzhao@hust.edu.cn

It thus attracts substantial attention from both the scientific community [1, 2] and engineering field such as automotive, aerospace and biomedical industries. Among the powder bed AM processes, selective laser melting (SLM) is still dominating [3, 4], while electron beam melting (EBM) is developing rapidly since it has potential to improve the productivity compared to SLM [5].

In addition to the advantages related to part geometry, the AM techniques also allow producing high strength materials with tensile strengths larger than their counterparts fabricated by traditional methods, such as casting and conventional powder metallurgy [3]. However, the production of metal AM parts for high demanding applications still faces challenges in terms of fatigue resistance. Indeed, the AM process generally leads to defects such as microstructure inhomogeneity [6], porosity [7, 8] and surface roughness [9, 10]; these defects are deleterious for material ductility and fatigue life. Moreover, during the layer by layer construction of the AM part, material experiences repeated thermal cycles which consist of rapid heating and cooling, leading to residual stresses (RS) [11]. It has been shown that tensile RS may reduce the fatigue life [12] and the fracture toughness [13], alter the fatigue crack growth rate [14] and eventually cause distortion or cracking of the manufactured part [15, 16], which degrade the accuracy or the integrity of the designed geometry.

As the heat history evolves in the building direction during the manufacturing, a non-uniform RS distribution is expected. Moreover, the RS level might depend on the AM technique (electron or laser beam based) as well as the metal to be manufactured (titanium, aluminum or steel). To understand the impact of the RS on mechanical performance, it is necessary to determine the RS level and distribution in the built part. To avoid ambiguity, the RS descriptions in both literature and the present work will follow the convention of coordinate system presented in Fig. 1.

In literature, many numerical works have been devoted to investigate the RS nature, level and distribution. In the framework of laser beam based AM processes, Matsumoto et al. [17] studied the temperature and stress within a single solidified metallic layer on the powder bed in selective laser melting (SLM) process. With two-dimensional (2D) finite element (FE) simulations, the authors showed that a large tensile stress between the solidified neighboring tracks would appear at the side end of the solid part, which may drive the in plane (xy plane) cracking of the layer. A three-dimensional (3D) thermal FE model was proposed by Fu et al. [18], which could capture the temperature gradient and thermal history in the multilayer buildup process

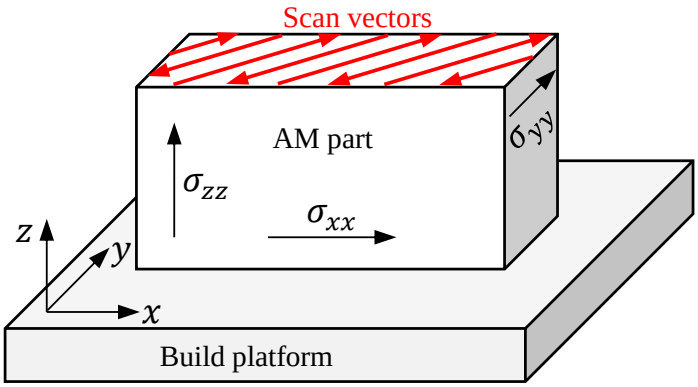

Figure 1: Convention of coordinate system in additive manufactured part. The directions x, y, z denote the longitudinal, transverse and building directions, respectively.

when simulating SLM Ti6Al4V. It was found that the temperature gradient in the depth direction (z direction) is much higher than that in width (y direction) and laser scanning (x direction) directions which could result in anisotropic residual stresses. Indeed, a more recent work [19] based on 2D thermomechanical simulations confirmed that the non-uniform temperature gradient led to anisotropic in plane (xy plane) residual stresses, i.e., the longitudinal component (σ_{xx}) was larger than the transverse component (σ_{yy}). Mukherjee et al. [20] proposed a 3D transient heat transfer and fluid flow model and predicted the RS distribution in large scale simulations (up to 16 mm in the building direction). The authors addressed the RS field in the whole modelled part (including the build platform), and showed that the RS level was higher in materials presenting a larger yield strength.

Regarding the electron beam based AM processes, numerical studies on electron beam melting (EBM) are still at a relatively early stage of development, compared to the SLM simulations [21], due to the fact that more physical mechanisms are involved during the EBM while less experimental data could be found in literature. Galati et al. [22] proposed a pure thermal model to mimic the electron energy source and simulate the thermal events involved in the EBM process. They recently implemented a fully coupled thermomechanical model and presented the thermal stress evolution as a function of time at a given point of a single track [23]. A similar investigation was documented by Vastola et al. [24] where they predicted the residual stress distribution for single-track electron beam melting of Ti6Al4V. They revealed that the RS level was highly dependent on the preheating temperature of the powder bed, each increase by 50°C resulting in a stress reduction by roughly 20% in the temperature range between 650°C and 900°C.

Concerning experimental studies, a variety of RS measurement techniques exist [25] and have been used to measure the RS level and distribution in SLM or EBM processed alloys [4]. The measurements can be categorized as local and global assessments according to the length scales, or as destructive and non-destructive according to whether they involve breaking the integrity of the sample or not. The typical local techniques are X-ray diffraction (XRD) and hole drilling strain gauge method (HDM). XRD was used to measure RS in a variety of SLM metals, for instance AISI 316L steel samples [26, 27], Ti6Al4V alloys [28, 29] or AlSi10Mg parts [30]. Although this technique could determine the local stress nature (tensile or compressive) and capture the influence of process parameters on RS, it does not allow assessing the RS distribution in the bulk material, given that XRD is limited to subsurface level and requires a polished surface. The hole drilling method (HDM) could overcome some of the above mentioned disadvantages. It allows conducting measurements at a deeper position from the surface and does not necessitate surface finishing. Using the HDM, Ali et al. [31] studied the correlation between the RS level and the scanning strategy for SLM Ti6Al4V; they showed that 90° alternating scanning strategy and re-scanning could result in significant reduction in residual stresses. Knowles et al. [15] showed that the HDM could be used to evaluate local RS on a complex geometry SLM Ti6Al4V specimen. They found that the residual stresses could locally approach the yield strength of the material. Moreover, the HDM can be used to assess the RS distribution in the hole drilling direction, as performed by [32, 33]. Nevertheless, the spatial resolution would be limited for the technique to be used for assessing large scale RS distribution in the building direction or the scanning direction, since the holes should be spaced far apart from each other to avoid interference.

Besides XRD and the HDM, another local approach, the instrumented indentation (II) technique, was used to assess the RS in both EBM Ti6Al4V and SLM Inconel 718 parts [34]. This technique shares however similar drawbacks with XRD and cannot be applied to measure RS distribution in bulk materials. When assessing a RS profile or field, more appropriate approaches should be employed. In recent years, newly emerging methods for residual stress measurement, such as digital image correlation (DIC) and laser ultrasonic technique, have been used for AM parts. Bartlett et al. [35] used three-dimensional DIC curvature measurements to monitor in situ in plane RS of SLM 316L steel. This technique is based on the intrinsic texture and contrast on the printed parts, which are captured by two cameras and converted to surface contours through 3D-DIC algorithms. It can be used generally in layer-by-layer deposition pro-

cesses such as spray coating [36, 37] and metal AM. The surface contours can be translated into stresses with an analytical model. The 3D-DIC is very appealing to assess instantaneous RS distribution in the current top layer during the AM process, but it cannot ensure the validity of measurements for previous building layers, since RS would be redistributed. Zhan et al. [38] applied the laser ultrasonic (LU) technique to measure RS in laser AM Ti6Al4V. Although this technique is capable of extracting a RS field, it is also limited to surface RS. Neutron diffraction (ND) offers a possibility of measuring internal stresses in bulk materials. Sochalski-Kolbus et al. [39] carried out neutron diffraction to measure RS in both EBM and SLM Inconel 718. They found that the maximum RS in the EBM sample was roughly 400 MPa lower than that in the SLM sample. Furthermore, neutron diffraction was used to measure RS in an SLM thin-walled structure made of Inconel 625 [40]. The authors revealed a stress (σ_{xx}) distribution such that the RS was low and compressive in the middle but high and tensile towards the two ends of the SLM part.

When assessing RS distribution in a particular direction, simple and fast measurements can be achieved by the crack compliance method (CCM) [41, 42] or the contour method (CM) [43]. Both techniques are based on the introduction of a crack which results in deformation or a crack surface contour that can be measured and used to compute the residual stresses. Mercelis and Kruth [11] proved the pertinence of assessing RS by CCM in SLM 316L steel. They found similar stress profile in the building direction as highlighted by neutron diffraction [40]. Vrancken et al. [14] and Ahmad et al. [44] applied the CM to assess RS in SLM Ti6Al4V; a similar conclusion was obtained in terms of stress profile.

From the above mentioned experimental works (summarized in Table 1), it can be seen that there are fewer experimental data for the EBM process compared to the SLM process. Despite numerous local assessments, the overall RS distribution in SLM parts was however insufficiently revealed. In particular, the effect of preheating the SLM build platform was rarely documented in literature. Moreover, to mitigate the intrinsic drawbacks related to the metal additive manufacturing process, such as residual stresses and porosity, it is necessary to perform post-treatments on the as built parts, prior to industrial applications. Heat treatment has been recommended as a systematic post-treatment process by SLM machine manufacturer [46, 47], as it dramatically enhances material ductility [45, 48, 49]. In contrast to heat treatment relieving residual stresses [45], thermomechanical post-treatments may alter the RS distribution in the AM part, which remains to be clarified. For example, friction stir processing (FSP) has been

Table 1: Summary of residual stress measurements of SLM and EBM parts in literature. XRD (X-ray diffraction), HDM (hole drilling method), II (instrumented indentation), DIC (digital image correlation), LU (laser ultrasonic), ND (neutron diffraction), CCM (crack compliance method), CM (contour method).

AM	Point measurement (method / material)	Field or line measurement (method / material)
SLM	XRD/316L [26, 27]/Ti6Al4V [12, 29]; XRD/AlSi10Mg [30, 45]; II/IN718 [34] HDM/Ti6Al4V [15, 31]/AlSi10Mg [33] HDM/AISI Marage 300 steel [32]	DIC/316L [35]; LU/Ti6Al4V [38]; ND/IN625 [40]/IN718 [39]; CM/Ti6Al4V [14, 44]/IN718 [44] CCM/316L [11];
EBM	XRD/Ti6Al4V [28]; ND/Ti6Al4V [7]; II/Ti6Al4V [34]	ND/IN718 [39]

shown to significantly improve microstructure [50], enhance tensile [6, 51] and fatigue [8] performance of SLM Ti or Al alloys, and eventually process AM metal based composites [52], but its impact on the RS should however be assessed to fully evaluate this post-treatment method. To compare the residual stresses for parts produced by different metal additive manufacturing techniques and post-processed by FSP, the present work deals with RS measurements in as built EBM Ti6Al4V, SLM Ti6Al4V, SLM AlSi10Mg and post-treated AlSi10Mg samples, using the crack compliance method. The CCM is chosen due to its simple implementation and capacity of assessing RS distribution throughout the whole sample. Our study is focused on the in plane RS (σ_{xx} in particular) level which has been found to be generally larger than the normal (building direction) RS level in both simulations [53, 54] and experimental measurements [29, 40].

2. Crack compliance method

2.1. Theory of the method

The crack compliance method (CCM) is dedicated to measure internal residual stresses within a bulk material. It is based on the measurement of deformation of the part when internal residual stresses are relieved by an artificially introduced crack [42], see Fig. 2. This method allows evaluating the RS distribution along the crack line, under the assumption that the stress is uniform throughout the sample thickness (for instance the direction perpendicular to the xy plane in Fig. 2).

The principle of the CCM is presented in Fig. 2. The uncracked and undeformed sample with residual stresses $\sigma_{rs}(x)$ can be equivalent to the deformed part due to crack introduction (by cut) plus a stress field applied to the crack face to force it returning to its undeformed shape. When the cut width is small compared to its length, the cut can be considered as a perfect crack so the analytical equations of the linear elastic fracture mechanics can be used to establish the relation between the residual stress and the strain at the measurement point M. In the framework of CCM for RS measurement, as the crack length is known, the measured strain can thus be used to calculate the load (residual stress).

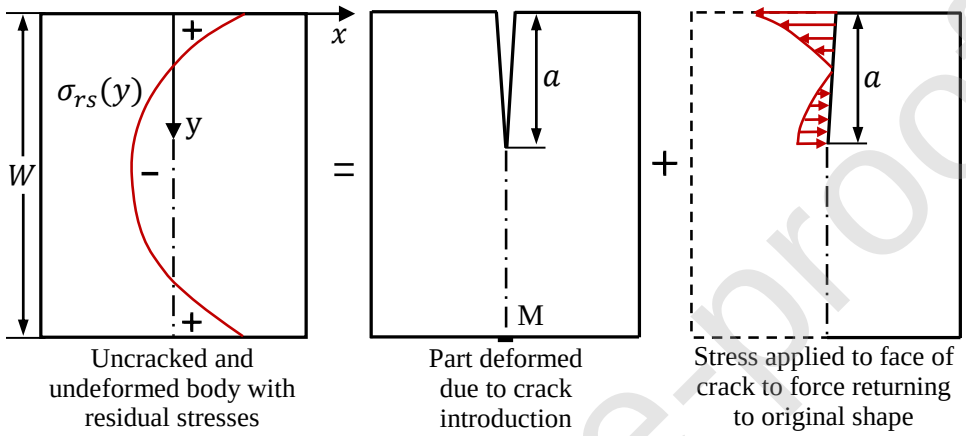

Figure 2: Schematic drawing replotted from [42] to present the principle of the CCM. M refers to the measurement point.

Practically, the relation between the measured strain and the residual stress is built through the stress intensity factor (SIF). According to [55], the SIF at the incrementally extended crack tip can be expressed as a function of strain change:

$$K_{Irs}(a) = \frac{E'}{Z(a)} \frac{d\varepsilon_M}{da} \tag{1}$$

Where E' stands for the generalized Young's modulus (i.e., $E' = E$ for plane stress condition and $E' = E/(1\text{-}\nu^2)$ for plane strain condition); $Z(a)$ is the so called influence function which only depends on the sample geometry, the crack plane and the location of the measurement point regardless of the residual stress distribution; ε_M denotes the strain measured by the strain gage (The subscript M represents the measurement point). The determination of $Z(a)$ for a rectangular sample with the strain gauge located at the rear surface is given in [41]:

$$Z(a) = \frac{-2.532}{(W-a)^{\frac{3}{2}}} \sqrt{1 - 25(\frac{a}{W} - 0.2)^2}[5.926(0.2 - \frac{a}{W})^2 - 0.288(0.2 - \frac{a}{W}) + 1] \tag{2}$$

When $\frac{a}{W} \leq 0.2$.

$$Z(a) = \frac{-2.532}{(W-a)^{\frac{3}{2}}} \tag{3}$$

When $0.2 < \frac{a}{W} < 1$.

On the other hand, the SIF can be expressed as a function of the residual stresses [55]:

$$K_{Irs}(a) = \int_0^a h(x,a)\sigma_{rs}(x)dx \tag{4}$$

Where $h(x,a)$ is the weight function as introduced by [56]; $\sigma_{rs}(x)$ denotes the residual stress along the crack plane and can be considered as the load to force the crack closure so that the sample returns to its uncracked shape. The weight function only depends on the geometry (including the crack length) of the sample. It can be found in literature for various cases [41, 42, 55]. According to Wu et al. [57], the weight function proposed by Wu and Carlsson [58] provides an accurate approximation of the SIF for a very large range of crack length ($0 < a/W < 0.9$). The expression of the weight function given by Wu and Carlsson [58] reads:

$$h(a,x) = \frac{1}{\sqrt{2\pi a}} \sum_{i=1}^{5} \beta_i(a) \left(1 - \frac{x}{a}\right)^{i-\frac{3}{2}} \tag{5}$$

The parameters β_i (i =1,2,3,4,5) are function of normalized crack length ($\xi = a/W$). Based on the work of Ribeiro and Hill [59], the parameters β_i are fitted and presented below:

$$\begin{aligned}
\beta_1(a) &= 2.0 \\
\beta_2(a) &= \frac{1}{(1-\xi)^{3/2}} \left(9.61\xi^6 - 57.57\xi^5 + 103.12\xi^4 - 93.58\xi^3 + 39\xi^2 - 0.53\xi + 0.96\right) \\
\beta_3(a) &= \frac{1}{(1-\xi)^{3/2}} \left(102.32\xi^6 - 218.51\xi^5 + 180.72\xi^4 - 58.65\xi^3 + 14.09\xi^2 - 2.93\xi + 1.16\right) \\
\beta_4(a) &= \frac{1}{(1-\xi)^{3/2}} \left(-139.42\xi^6 + 304.94\xi^5 - 262.76\xi^4 + 100.3\xi^3 - 17.84\xi^2 + 1.76\xi - 0.37\right) \\
\beta_5(a) &= \frac{1}{(1-\xi)^{3/2}} \left(51.25\xi^6 - 113.6\xi^5 + 100.08\xi^4 - 40.66\xi^3 + 7.49\xi^2 - 0.26\xi - 0.08\right)
\end{aligned} \tag{6}$$

From the experimentally determined $K_{Irs}(a)$ with measured deformation, it is possible to calculate the initial residual stress distribution, $\sigma_{rs}(x)$, by inversion of Eq. 4, as will be presented in the following section.

2.2. Computation procedure

The computation of residual stresses is stepwise as the crack extension is incremental. The deformation for every crack extension Δa is recorded. After calculating the stress intensity factor with Eq. 1, the residual stresses σ_{rs} can be calculated using Eq. 4. For the first cut increment (i.e., the range $0 < x < a_1$), the stress level, denoted by σ_1, can be easily calculated from the well known relation between the SIF and the stress for a short edge crack [60]:

$$\sigma_1 = \frac{K_{Irs}(a_1)}{1.12\sqrt{\pi.a_1}} \tag{7}$$

Then, it is possible to compute σ_2 corresponding to the crack extension from a_1 to a_2 ($a_2 = a_1 + \Delta a$):

$$K_{Irs}(a_2) = \sigma_1 \int_0^{a_1} h(x, a_2)dx + \sigma_2 \int_{a_1}^{a_2} h(x, a_2)dx \tag{8}$$

Therefore, the average stress σ_i in the range $a_{i-1} < x < a_i$ can be obtained by the following equation:

$$K_{Irs}(a_i) = \sigma_1 \int_0^{a_1} h(x, a_i)dx + \sum_{j=2}^{i-1} \sigma_j \int_{a_{j-1}}^{aj} h(x, a_i)dx + \sigma_i \int_{a_{i-1}}^{ai} h(x, a_i)dx \tag{9}$$

Using Eqs. 7 and 9, the residual stress σ_i versus the cut depth a_i can therefore be computed.

3. Materials and experiments

3.1. Material manufacturing

3.1.1. Electron beam melting Ti6Al4V

The manufacturing of the EBM Ti6Al4V samples was conducted with the Arcam A2 EBM machine. The build platform, provided by the machine manufacturer, is made of stainless steel and has a dimension of 210×210×10 mm. The samples were rectangular plates with a dimension of 150 mm × 35 mm × 5 mm. 35 mm corresponds to the dimension in the building direction. Two samples were manufactured with the standard parameters optimized for the layer thickness of 50 µm: a focus offset (FO) of 3 mA, a speed function (SF) of 98. Note that the FO denotes the current used by the focusing coils to focus the electron beam, the SF controls the beam speed as a function of the current so that a constant melt depth is maintained. The

powder was heated up to 850°C for each layer before being melted by the electron beam. During the hatching, the electron beam moves parallel to the principal directions of the machine (x' or y'), and rotates 90° between layers. The samples built with the standard parameters are oriented 45° with respect to the principal axes of the beam scanning (machine coordinate system (x', y', z') in Fig. 3) so that the scanning length is the same after the rotation of 90°of the electron beam. To evaluate the effect of the parameters on the residual stresses, the FO and SF were changed for two additional samples. Note that the change of FO will change the spot size, thus the energy density of the electron beam, while the variation of SF will alter the melt pool depth [21].

The four samples, two built with standard parameters and two with modified parameters, were made in the same batch: two samples with standard parameters (the same used by de Formanoir et al. [61], FO = 3 mA, SF = 98, layer thickness = 50 µm, line offset = 100 µm), named as EBM-Ti-STD1 and EBM-Ti-STD2; one sample with modified speed function (FO = 3 mA and SF = 60), referred to as EBM-Ti-FO03-SF60; one sample with modified focus offset (FO = 14 mA and SF = 98), named EBM-Ti-FO14-SF98.

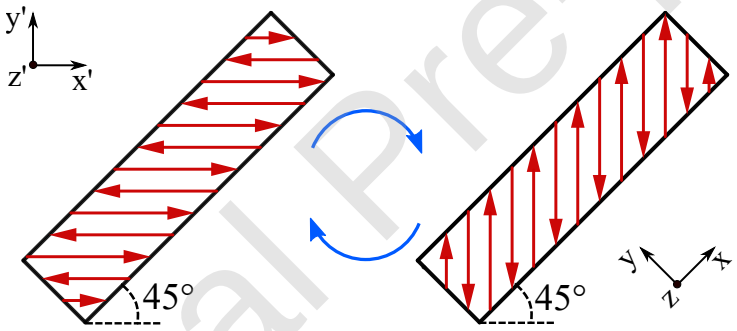

Figure 3: Orientations of the EBM parts on the hatching pattern, with the electron beam moving along the principal directions (x' and y' axes). The built sample is oriented 45° with respect to principal axes. The red straight arrows denote the scanning direction of the electron beam, the blue curved arrows indicate that the electron beam rotates 90° between layers. The coordinate systems (x', y', z') and (x, y, z) are associated to the EBM machine and the built samples respectively.

3.1.2. Selective laser melting Ti6Al4V and AlSi10Mg

Two different SLM materials, Ti6Al4V and AlSi10Mg, were studied. Both were manufactured with an EOS M290 machine with the machine manufacturer suggested parameters. The build platform has a dimension of 252×252×25 mm. It is made of Ti6Al4V alloy and EN AW 5083 aluminium alloy for the production of Ti6Al4V and AlSi10Mg samples, respectively. The processing started with building a reticulated support and then continued with the desired part

(see Supplementary material, section 1). All the SLM samples share the same geometry with the EBM samples. The SLM Ti6Al4V samples were built with the "Ti64_Performance_M291 1.10" parameters delivered by the machine manufacturer EOS [47], which sets the layer thickness to 30 µm. A rotation of 67° was conducted between layers, see Fig. 4. The build platform temperature was 35°C. The Ti6Al4V sample was named SLM-Ti-35C. The SLM AlSi10Mg samples were built with the EOS parameters "AlSi10Mg_Speed 1.0" [46] and "AlSi10Mg_200C" [62] (with layer thickness equal to 30 µm and scan rotation equal to 67°for both), which set the build platform temperature to 35°C and 200°C, respectively. The two different temperatures will allow to evaluate the effect of preheating on the RS level. The corresponding samples were named SLM-Al-35C and SLM-Al-200C, respectively.

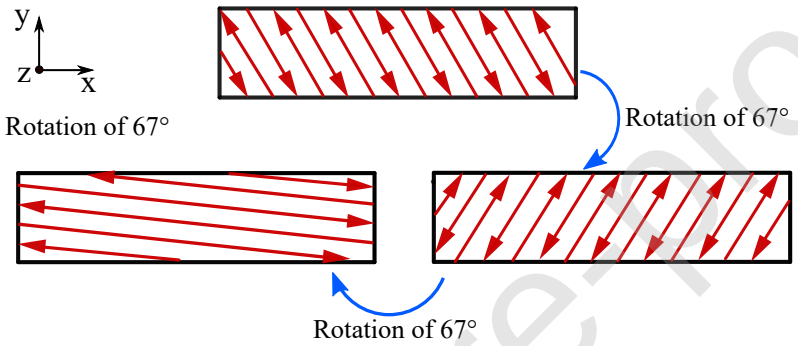

Figure 4: Orientations of the SLM parts with respect to the hatching pattern, with the laser beam rotating 67° between layers, as indicated by the blue curved arrows. The red straight arrows denote the scanning direction of the laser beam. Note that the schematic just shows the rotation of the scanning direction between layers, the angle of 67° does not allow full hatching repetition.

3.1.3. Friction stir processing of SLM AlSi10Mg

To assess the residual stresses generated by FSP, as this post-treatment has been proven to highly enhance fatigue life of SLM AlSi10Mg alloy [8], two SLM-Al-200C plates were friction stir processed (FSPed) nearly throughout the thickness. FSP was conducted with a conventional milling machine. The backing plate and the clamping system were installed in a tank containing cutting oil, which allows increasing the cooling rate. The used FSP tool was composed of a scrolled shoulder of 20 mm in diameter and a pin of 6 mm in diameter and 4.6 mm in length. One single FSP pass was performed in the center of the sample with a rotational speed of 1000 rpm and a traverse speed of 500 mm/min. The FSPed samples are referred to as SLM-Al-200C-FSP.

3.1.4. Chemical composition

The chemical compositions of the built samples were measured by the inductively coupled plasma optical emission spectroscopy (ICP-OES) technique and are given in Table 2 and 3. The chemical compositions are consistent between the EBM-Ti and the SLM-Ti-35C samples, as well as between the SLM-Al-35C and the SLM-Al-200C samples.

Table 2: Chemical composition in wt.% of the EBM-Ti and SLM-Ti-35C samples.

	Ti	Al	V	Fe
EBM-Ti	Bal.	5.87	3.97	0.20
SLM-Ti-35C	Bal.	5.96	4.05	0.17

Table 3: Chemical composition in wt.% of the SLM-Al-35C and SLM-Al-200C samples.

	Al	Si	Mg	Fe
SLM-Al-35C	Bal.	9.68	0.43	0.13
SLM-Al-200C	Bal.	9.60	0.43	0.14

3.2. Mechanical strength characterization

Before assessing the residual stresses of the above mentioned materials, uniaxial tensile tests were performed to characterize their mechanical strength and to evaluate the relative residual stress levels. For the EBM Ti6Al4V alloy, only the samples built with the standard parameters were tested for mechanical performance, given that the variation in focus offset and speed function does not remarkably affect the mechanical strength [61]. Horizontally oriented (with regard to the SLM building platform) round tensile specimens were extracted by machining from the as built plates and from the FSP center zone. The locations where the tensile specimens were cut from the samples are illustrated in Supplementary Fig. 2. The tests were carried out with a Zwick tensile machine, using a gauge length of 25 mm and a loading rate of 1 mm/min. At least two samples were tested for each material to ensure the reproducibility of the tests.

3.3. Residual stress measurements

Prior to performing the residual stress measurements, the built plates were detached from the build platform. Two additional SLM-Al-200C samples were friction stir processed. The strain gauge was glued at the center of the rear surface for all the samples. The top surface was selected as the rear plane (see Fig. 5) as the bottom surface was too rough and could have caused distortion of the strain gauge. The attachment of the gauge is depicted in supplementary material, section 3. Correspondingly, the cutting was planned to start from the center of the bottom surface and was maintained perpendicular to the rear surface. The bottom-to-top profile of the residual stresses in the x axis (σ_{xx}) was thus measured. Note that the x axis is consistent in all the figures of the present work.

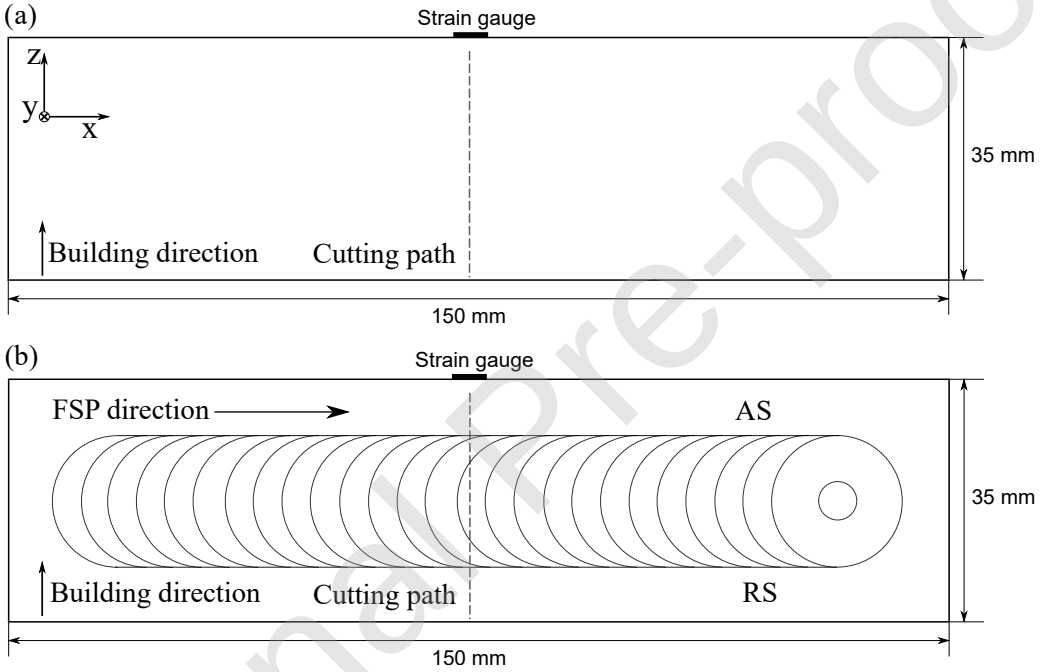

Figure 5: Sketch of the CCM sample incorporating the strain gauge as well as the pre-defined cutting path. As built AM samples (a), FSPed samples (b). AS and RS in (b) denote the advancing side and retreating side of FSP, respectively.

Electron discharge machining (EDM, Agie Charmilles Cut 20P) was used to extend the crack step by step. The wire diameter was around 250 μm, and the induced crack width was around 400 μm. As presented in Fig. 6, the sample was mounted at one edge in the machine clamping system, using a single screw, to avoid any constraint against the deformation generated by the RS relief. The crack extension was incremental, the wire advanced 1 mm for each step for all the as built samples. However, a refinement of cut, i.e., a step of 0.5 mm, was performed in the FSP stir zone (from 8 mm to 27 mm), since it has been shown that this region could

exhibit complex RS distribution [63, 64, 65]. Every subsequent cut was launched when the strain gauge signal became stable after the previous extension. The final crack length was 33 mm; the crack tip was thus 2 mm away from the attached strain gauge.

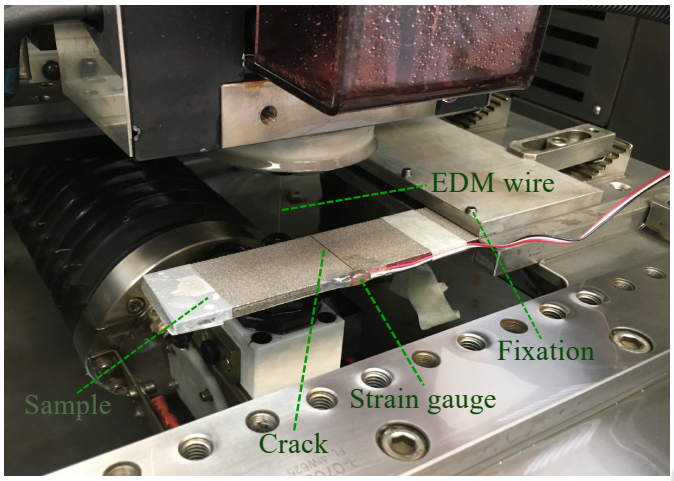

Figure 6: Mounting of the sample in the EDM machine.

4. Results

4.1. Mechanical strength

The engineering tensile curves are presented in Fig. 7. The yield strengths of the EBM-Ti-STD and the SLM-Ti-35C samples are 1020±7 MPa and 1150±12 MPa, respectively. The SLM process imparts higher strength but lower ductility compared to the EBM process (see Fig. 7a). Regarding the SLM AlSi10Mg alloy, the SLM-Al-35C, SLM-Al-200C and SLM-Al-200C-FSP present a yield strength of 287±2 MPa, 200±2 MPa and 189±3 MPa, respectively. Interestingly, it is found that the preheating of build platform leads to both lower strength and ductility (see Fig. 7b). The FSP post-treatment brings about a significant increase in ductility, accompanied by a slight decrease in strength.

Note that the tensile tests probe the material properties in the same direction as the residual stresses (the x direction in Fig. 5). The mechanical strength of the sample can thus serve as a reference for the residual stress level.

4.2. Residual stress distribution

The residual stress measurements covered the as built EBM Ti6Al4V, SLM Ti6Al4V, SLM AlSi10Mg and post-treated AlSi10Mg samples. The results allow to assess the effect of the AM process, the material properties, the preheating as well as the post-treatment on the RS level and

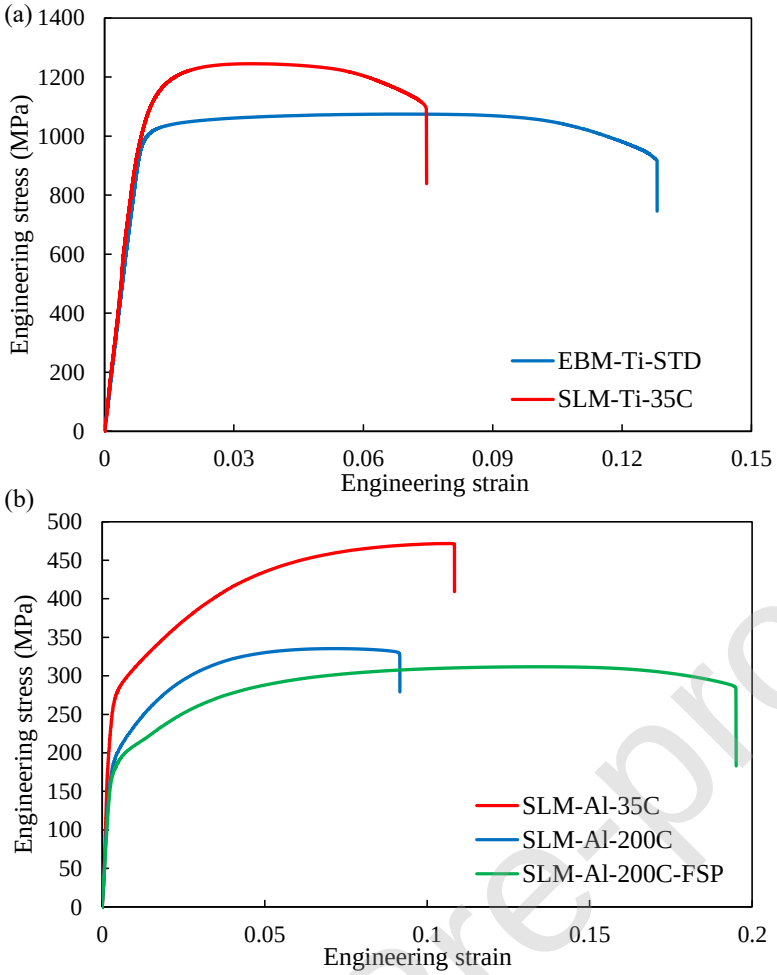

Figure 7: Tensile curves of the studied materials. (a) EBM-Ti-STD and SLM-Ti-35C samples, the elongation to fracture is 0.13±0.009 and 0.07±0.003 for the EBM-Ti-STD and SLM-Ti-35C, respectively, (b) SLM-Al-35C, SLM-Al-200C and SLM-Al-200C-FSP samples, the elongation to fracture is 0.11±0.007, 0.095±0.004 and 0.18±0.01 for the SLM-Al-35C, SLM-Al-200C and SLM-Al-200C-FSP, respectively. Note that the tensile tests were well reproducible and only one representative curve is presented for each material.

distribution. The data of measured strain versus cut depth for all the tested samples are provided in supplementary material (see Supplementary material, section 4). It should be noted that only the longitudinal residual stresses (σ_{xx}) are assessed.

4.2.1. EBM Ti6Al4V

The residual stress profiles of the EBM Ti6Al4V are presented in Fig. 8. It is noticeable that the residual stresses are nearly negligible in all the measured samples. The very low RS level is coherent with the relatively small strain values measured by the strain gauge (see Supplementary Fig. 4). The change in the focus offset from 3 mA to 14 mA brings no impact on the RS. The decrease in the speed function from 98 to 60 seems to increase slightly the RS at the top of the

built part, however, the absolute RS level remains extremely low compared to the yield strength of the EBM-Ti-STD sample which is 1020 MPa, as mentioned in section 4.1. Therefore, it can be concluded that the EBM process results in nearly RS free Ti6Al4V alloy in the present work.

In literature, the residual stresses in EBM samples were mostly assessed by the X-ray diffraction or neutron diffraction methods. Edwards et al. [28] revealed that the residual stresses were nearly zero at the center of the top and bottom planes of the EBM Ti6Al4V samples. Hrabe et al. [7] also showed that the RS level was very low (the RS values are in the same order of magnitude as the standard error of 30 MPa) in EBM Ti6Al4V. Sochalski-Kolbus et al. [39] evaluated the RS in Inconel 718 built by both EBM and SLM. They revealed that the maximum RS in the EBM samples was 400 MPa lower than that in the SLM samples. Therefore, the results in the present work are in line with previous studies.

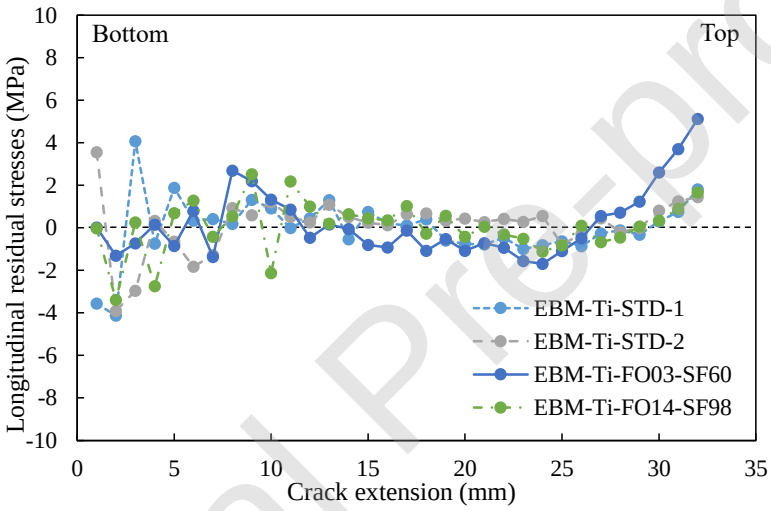

Figure 8: Residual stress profiles in the EBM Ti6Al4V manufactured with different focus offsets and speed functions. The position of x=0 corresponds to the bottom surface of the built plate.

4.2.2. SLM Ti6Al4V

Regarding the SLM Ti6Al4V samples, the two measurements present an excellent reproducibility. The built samples exhibit compressive stresses in the center region and tensile stresses at the top and the bottom (see Fig. 9). Note that the zero crack extension corresponds to the bottom surface of the sample. This RS profile is qualitatively coherent with the theoretical prediction [11] as well as the measurement by the contour method [14] for the SLM process. The maximum tensile stress is around 250 MPa and the maximum compressive stress is roughly -200 MPa, or 22% and 17% of the yield strength, respectively. The RS profile is not strictly symmetric along the building direction, as the valley of the profile is closer to the top plane of

the sample. Moreover, it can be expected that the RS at the top plane would be higher than that at the bottom plane if an extrapolation was done to extend the cut to 35 mm. This particular distribution shape does not match perfectly well with the predicted one given by the simplified theoretical model [11], which reveals a quasi symmetric RS distribution, with the valley of the stress profile slightly shifting towards the bottom of the sample when adding more layers to the part.

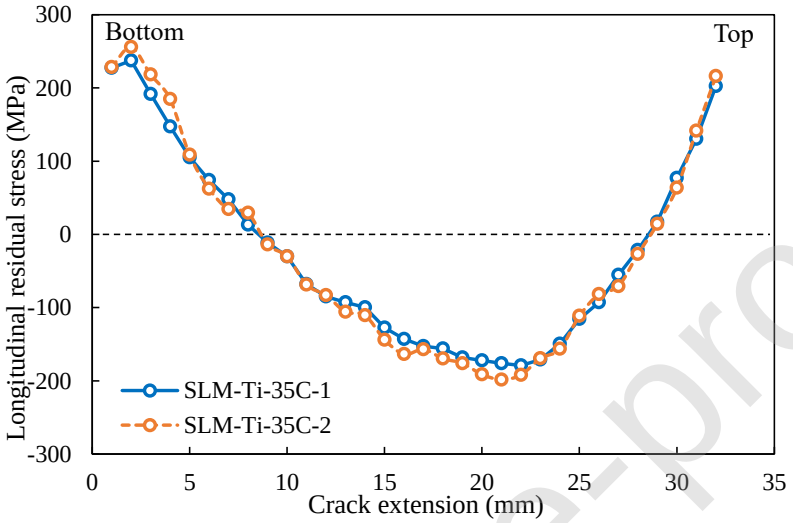

Figure 9: Residual stress profiles in the SLM Ti6Al4V. The position of x=0 corresponds to the bottom surface of the built plate.

Quantitatively, the tensile stresses at both the top and the bottom are close to what has been obtained by the X-ray diffraction method (top: 200 MPa, bottom: 260 MPa) in a previous investigation [12]. However, the XRD data for the central region was not reported in literature. Indeed, the crack compliance method used here allows easily assessing the stress evolution throughout the building direction, which would require much heavier work with X-ray diffraction.

4.2.3. SLM AlSi10Mg

The residual stresses of the SLM AlSi10Mg with the two build platform temperatures are plotted together in Fig. 10 to have a direct comparison. The good reproducibility also ensures the reliability of the assessment for each condition. It can be noticed that the RS in the SLM-Al-35C shares the distribution profile with the SLM-Ti-35C. The discrepancy lies on the fact that the valley is more shifted towards the top part of the SLM-Al-35C sample. The maximum tensile stress is around 50 MPa and the maximum compressive stress is approximately -41 MPa,

or 17% and 14% of the yield strength, respectively.

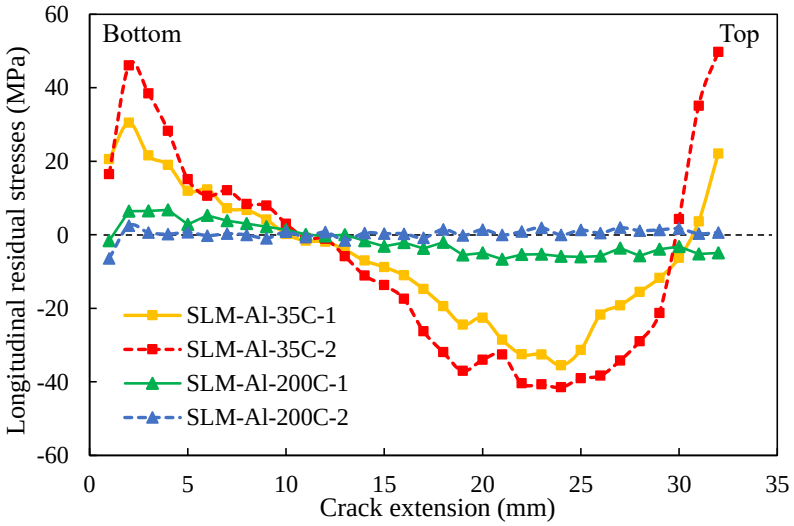

Figure 10: Residual stress profiles in the SLM AlSi10Mg with build platform temperatures of 35°C and 200°C. The position of x=0 corresponds to the bottom surface of the built plate.

Regarding the SLM AlSi10Mg manufactured with the build platform preheated to 200 °C, the measured residual stresses are lower than 5 MPa, indicating that the preheating leads to significant RS mitigation during the SLM process. The order of magnitude of the peak stress level for both building conditions of the SLM AlSi10Mg samples (35°C and 200°C) is in good agreement with the measurements performed by X-ray diffraction: 40-80 MPa at the center of the sample top surface for the build platform at room temperature [30]; around ± 7 MPa in the sample top plane for the build platform heated to 200 °C [45].

4.2.4. Effect of friction stir processing

Friction stir processing has been recently applied to AM parts as a post-treatment method, leading to superior tensile properties [6] and fatigue performance [8]. From Fig. 10, it is known that the SLM-Al-200C plate is nearly RS free before FSP. The residual stresses in the SLM-Al-200C-FSP samples are thus completely generated by the post-treatment. Fig. 11 presents the induced RS distribution after 1 FSP pass. The ”M” shape, as typically seen in FSPed aluminum samples [63, 64, 65], is observed: the FSP stir zone presents relatively low tensile stresses (<50 MPa); the tensile stresses increase towards the two sides of the sample and reach a maximum (around 100 MPa) near the FSP tool shoulder edge; the residual stresses then decrease and become compressive (-125 MPa) near the two edges of the FSPed sample. It should be noted that if the sample had been wide enough, the residual stresses would have decreased to zero far

from the FSP stir zone, as revealed by Lombard et al. [64].

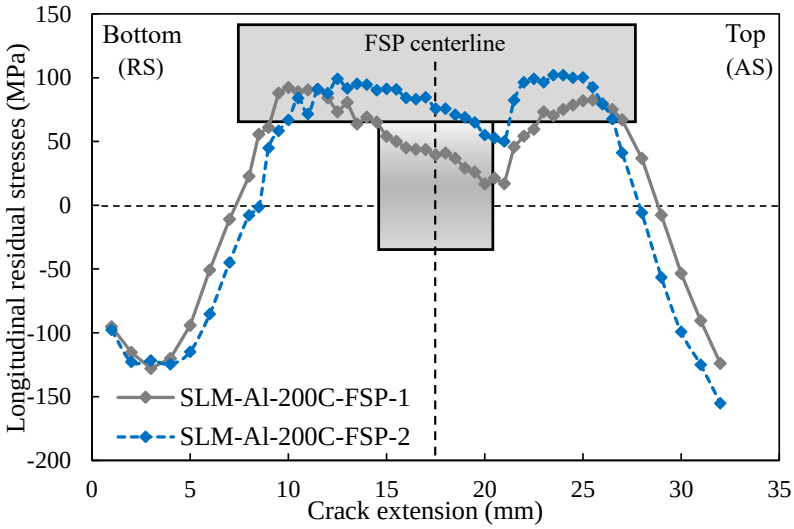

Figure 11: Residual stress profiles in the FSPed SLM AlSi10Mg manufactured with build platform temperature of 200°C. The position of x=0 corresponds to the bottom surface of the built plate. AS and RS denote the advancing side and retreating side of FSP, respectively. The shoulder and the pin of the FSP tool are represented to highlight the RS distribution with respect to the FSP zone.

Considering the mechanical properties of the SLM-Al-200C, the maximum tensile residual stress in the FSPed sample reaches approximately 50% of the yield strength of the base material. This ratio falls well in the range between 42% and 53% measured in the friction stir welded Al6082-T6 alloy (with various process parameters) presenting a similar yield strength (241 MPa) [65].

5. Discussion

As one of the key issues hindering the widespread application of the metal powder bed fusion additive manufacturing parts, residual stresses have received extensive attention. Through the crack compliance method, we provide here an overall estimation of the RS distribution along the building direction of both the electron beam melting and the selective laser melting processes, involving the two widely studied alloys in the AM community, i.e., Ti6Al4V and AlSi10Mg. The obtained stress profiles and levels are in qualitative agreement with the theoretical predictions and close to the reported values estimated by other measurement methods, as summarised in Table 4. The good agreements therefore build a solid ground for discussion as follows.

It is widely accepted that residual stresses are generated due to high cooling rate and strong

Table 4: Comparison of residual stresses measured by the crack compliance method in the present work with residual stresses measured by X-ray diffraction reported in literature. The measurements were all conducted on samples removed from build platform.

Material	Position	RS value in this work (MPa)	Ref. RS value (MPa)	Reference
EBM-Ti	Bottom center	0.2	0	[28]
SLM-Ti-35C	Bottom center	220	260	[12]
SLM-Al-35C	Top center	50	40-80	[30]
SLM-Al-200C	Top surface	-5	±7	[45]

a. The preheating temperature of the EBM process was 700°C in [28];

b. The parameters used in [12]: laser power of 200 W, layer thickness of 50 μm, scan rotation of 67°C;

c. The parameters used in [30]: laser power of 400 W, layer thickness of 50 μm, horizontal sequential pattern;

d. The preheating temperature of build platform of the SLM process was 200°C in [45].

thermal gradient during manufacturing [11, 66]. As presented in the schematic drawing in Fig. 12, a steep thermal gradient is developed during the rapid heating, leading to much larger thermal expansion at the upper layers; during the rapid cooling, the upper layers shrink very fast due to thermal contraction, which will be inhibited by the underlying layers, thus inducing longitudinal tensile stress in the current layer and longitudinal compressive stress below. With the layer accumulation, the RS will be redistributed in a way that the compressive stresses are generally present in the build platform, while the built part exhibits tensile stresses [11]. In the present work, it is found that preheating significantly mitigates RS, regardless of preheating every layer of powder (EBM-Ti, Fig. 8) or only the build platform (SLM-Al-200C, Fig. 10). The RS mitigation is expected to result from reduction of cooling rate and thermal gradient due to temperature increase of the underlying material. Post-fabrication heating can also reduce or eliminate the residual stresses, aiming at improving the fatigue life, as practiced in previous works [8, 67]. However, preheating the build platform also leads to accurate geometry [68] which cannot be achieved by thermal post-treatments.

Although preheating grants negligible RS, the relatively smaller cooling rate leads to lower tensile strength compared to the selective laser melting metal, as can be seen from comparison between the EBM-Ti-STD and SLM-Ti-35C as well as between the SLM-Al-35C and SLM-200C in the present work (see Fig. 7). The higher strength of the SLM Ti6Al4V has been

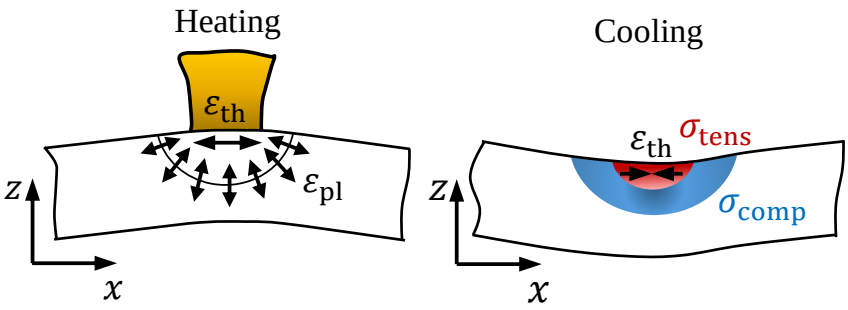

Figure 12: Formation mechanism of residual stresses in metal additive manufacturing. The arrows indicate the nature of thermal deformation (thermal expansion in the left schematic and thermal contraction in the right schematic).

explained by the finer α' martensite phase [69]. To understand the effect on preheating of build platform in the SLM process, the microstructure has been characterized for the SLM-Al-35C and SLM-Al-200C samples, as presented in Fig. 13. The preparation for the metallurgical observations follows the same procedure of our former work [51], and the observations were conducted with a scanning electron microscope (SEM). It can be noticed that the preheating leads to a coarser microstructure, in the sense that the Si-rich eutectic network is thicker and the precipitates in the α-Al cell are larger in the SLM-Al-200C compared to the SLM-Al-35C. Note that the precipitates mainly contain Si for both build platform temperatures, as evidenced by TEM characterization of materials built with the same SLM parameters [51, 70]. As discussed by Zhao et al. [51] and Maconachie et al. [71], the failure of the as built SLM AlSi10Mg alloy is mainly controlled by the fracture of the Si-rich eutectic network; when the brittle network is coarser, it fractures earlier as observed in [71], resulting in lower ductility.

Moreover, preheating might also play a role on porosity level; note that EBM Ti6Al4V has been shown to present lower porosity than SLM Ti6Al4V [69]. In order to assess the influence of preheating the SLM build platform and the FSP post-treatment on porosity level, X-ray computed tomography has been carried out on the SLM-Al-35C, SLM-Al-200C and SLM-Al-200C-FSP (FSP stir zone) samples (more details of the tomography study are given in section 5 of the supplementary material). A voxel size of 1.6 µm was used to have a large scanned volume so that big pores (more dangerous for fatigue life than small pores) are more likely captured. The 3D visualization of porosity is presented in Fig. 14; the pores are found to be larger in the SLM-Al-35C sample. It should be noted that no pores have been observed in the SLM-Al-200C-FSP sample, confirming the capacity of eliminating porosity by FSP. After a size

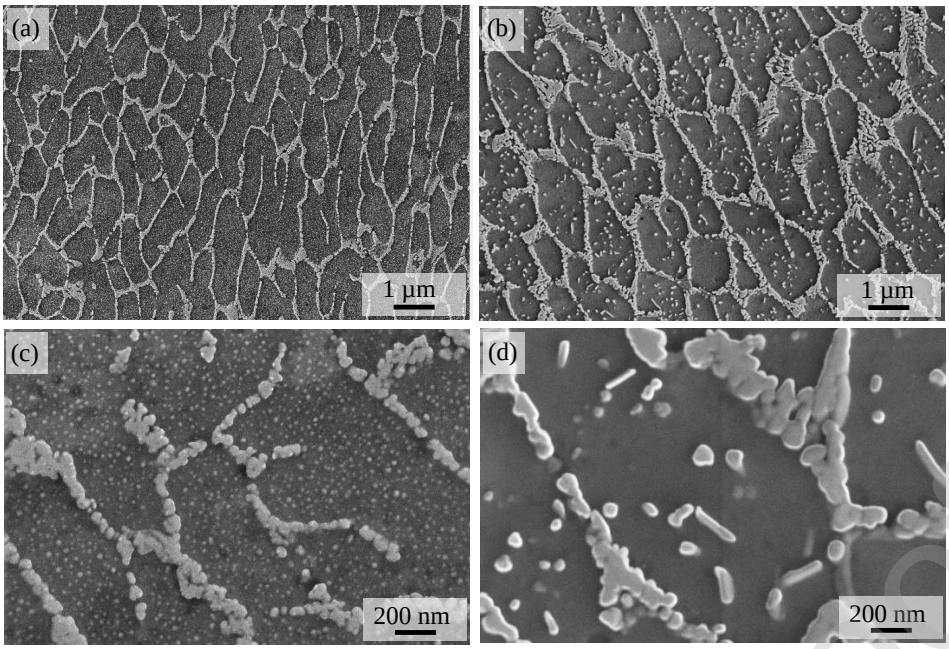

Figure 13: Microstructure observations (with SEM) of the SLM AlSi10Mg samples. Morphology of the Si network in the SLM-Al-35C (a) and SLM-Al-200C (b), observation of fine precipitates in the α-Al cells of the SLM-Al-35C (c) and SLM-Al-200C (d).

thresholding that excludes objects smaller than 5 voxels, only pores larger than 3.4 µm (equivalent diameter) are counted in the statistics. The pore volume fraction of the SLM-Al-35C sample (0.039%) is found to be larger than that of the SLM-Al-200C sample (0.016%). From the pore size distribution (Fig. 15), it is also observed that there exist much bigger pores in the SLM-Al-35C sample. Therefore, preheating turns out to be beneficial for porosity mitigation and presents potential to enhance fatigue resistance of SLM metals. It has been widely recognized that porosity in AM part involves two main sources, gas trapping (porous powder, moisture, vaporization) and lack of fusion (particle spattering, insufficient melting) [72, 73]. Preheating reduces the cooling rate, thus leading to higher temperature of the powder layer to be melted at the ongoing laser scanning step. It can therefore be expected that the residual heat from the previously built layers evaporates the remaining moisture, enhances the gas diffusion, reduces the particle spattering via heat induced presintering [74, 75] and promotes the melting of the current powder layer, thus leading to lower porosity. Extended investigations are needed in the future to assess this point, using advanced in situ monitoring techniques, such as full-field infrared (IR) thermography [76], 3D-DIC [77] and high-speed high-energy X-ray imaging [74].

When no preheating is involved in the SLM process, the Ti6Al4V sample is found to exhibit higher RS level than the AlSi10Mg sample, though the distribution profiles are similar. This

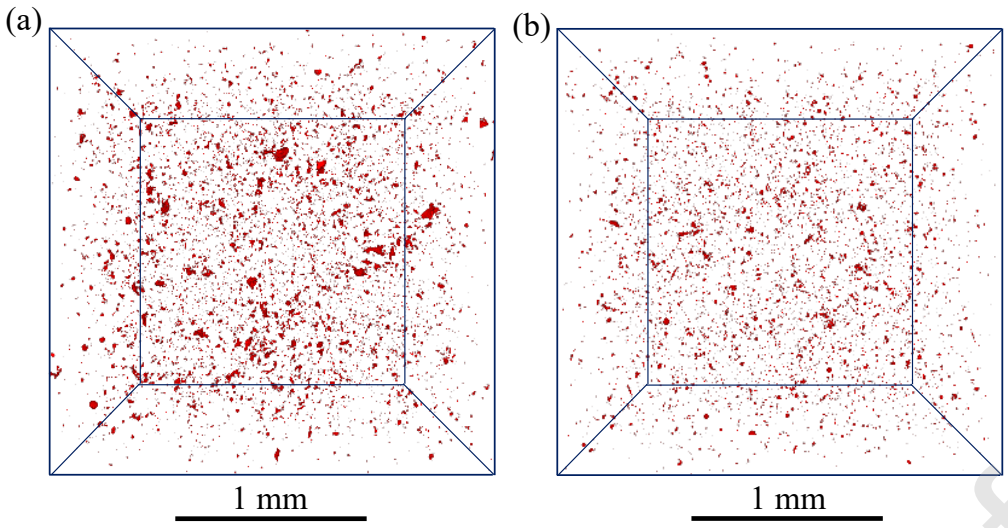

Figure 14: 3D visualization of porosity in the SLM-Al-35C (a) , and the SLM-Al-200C (b) samples.

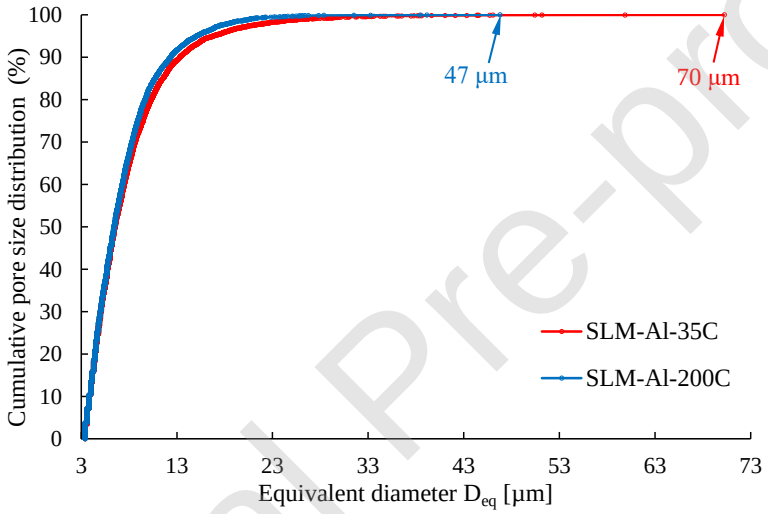

Figure 15: Cumulative pore size distribution (volume weighted) in the SLM-Al-35C and SLM-Al-200C samples. The voxel size is 1.6 µm, the pore statistics are performed in a cube presenting an edge length of 2.24 mm for both samples.

is in line with the theoretical analysis [11] which predicted larger residual stresses in materials presenting higher mechanical strength. However, when normalizing the residual stress over the yield strength, it is found that the relative RS level is close between the SLM-Ti-35C and SLM-Al-35C: 22% vs. 17% for the maximum tensile RS and 17% vs. 14% for the maximum compressive RS.

It should be noted that the residual stresses measured in the present work result from the re-equilibrium of force and momentum after the sample removal from the build platform. Mercelis and Kruth [11] showed that the residual stresses could be one order of magnitude larger

before sample removal. The removal involves thus a stress relaxation which can deform the built part and degrade its geometrical accuracy. As presented in Fig. 16a-b, SLM samples generally present tensile residual stresses after being manufactured on the build platform, with the platform constraint represented by a tensile and a bending load on the bottom plane of the sample (green arrows in Fig. 16a). The detachment of the part can thus be considered as acting a reverse load on the bottom plane, which is translated into a uniform shrinkage (Fig. 16c) and a bending deformation (Fig. 16d) of the part. The combination of the initial tension, the uniform shrinkage and the bending leads to the final residual stress distribution in the detached part (Fig. 16e).

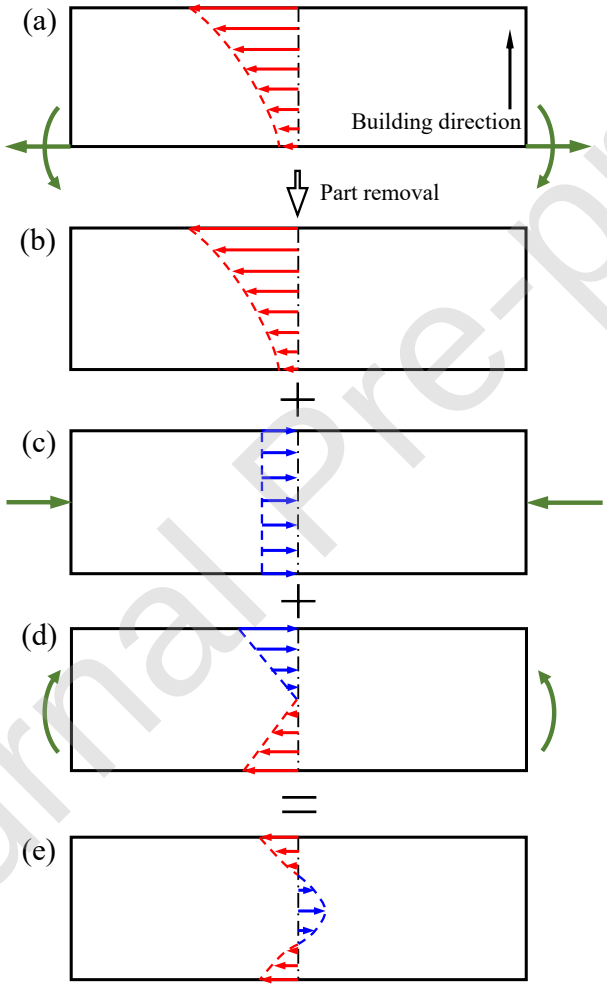

Figure 16: Redistribution of residual stresses upon part removal from the build platform. Initial tensile stresses and constraint from the build platform (a), initial tensile stress distribution (b), uniform shrinkage upon part removal (c), bending deformation upon part removal (d), final residual stress distribution after part removal (e). The red and blue arrows represent tensile and compressive stresses, respectively.

From the above analysis, it can be seen that the asymmetry of the measured RS profile (see

Figs. 9 and 10) should result from the initial tensile stress distribution (Fig. 16b), which might change with the build platform structure. It should be noted that the prediction in [11] was based on a solid build platform, while in the present work, the SLM parts were built on a reticulated support (see Supplementary Fig. 1). This difference might explain why the RS minimum peak shifts to the top plane in the present measurements, while it is nearly in the center of the sample in the prediction [11]. More work needs to be done in the future to investigate the effect of adding reticulated support compared to building directly on the solid platform.

Regarding the FSP post-treatment of the SLM AlSi10Mg incorporating a 200°C preheating, the residual stresses are even larger than that in the as built SLM AlSi10Mg without preheating. FSP generates heat and leads to local temperature rise up to 80% of the melting point [78]. Residual stresses arise due to a relatively high cooling rate and strong thermal gradient. Despite the relatively high tensile residual stresses in the FSP stir zone, the porosity can be highly reduced because of the intense plastic deformation, as reported by Santos Macías [8] and confirmed in the present work with the X-ray computed tomography measurement (no pores have been observed in the FSP stir zone). Accordingly, FSPed SLM AlSi10Mg alloy has been shown to exhibit much longer fatigue life compared to both the as built (without preheating) and the stress relieve heat treated (SRHT) states [8]. This indicates that the porosity is expected to be more dangerous than the relatively low residual stresses (20% of the yield strength) to fatigue resistance in SLM metals. Indeed, the residual stresses would be partly released and redistributed during machining of fatigue test specimens. However, the RS level, in particular for specimens extracted from the center of the as built (compressive RS, Fig. 10) or FSPed (tensile RS, Fig. 11) SLM plates, is more likely higher in the FSPed state than in the as built and SRHT states. The quantification of RS in mechanical test specimens cannot be assessed by the CCM method; X-ray diffraction or neutron diffraction would be supportive approaches to verify the aforementioned conjecture and to measure the RS level in the prepared specimens.

6. Conclusions

In this paper, the crack compliance method is used to assess the in-plane (scanning plane) residual stress distribution along the building direction in both the EBM and SLM samples. The investigations cover two widely studied AM alloys for direct comparison, i.e., Ti6Al4V and AlSi10Mg. The impact of preheating of SLM build platform on residual stress level is evaluated. Moreover, the redistribution of residual stresses by friction stir processing is unveiled

to further evaluate this post-treatment technique showing ability to suppress initial porosity. The main findings are:

(1) The crack compliance method is an efficient and simple way to estimate the overall residual stress distribution in simple geometry AM parts, results are highly reproducible;

(2) The residual stresses are found to be negligible in both the EBM and SLM samples incorporating a preheating step, due to the mitigation of cooling rate and thermal gradient;

(3) The SLM samples excluding preheating step present tensile stresses at the top and the bottom of the sample and compressive stresses in the center. The normalized RS levels in the Ti6Al4V and AlSi10Mg are close and generally lower than 22% of the yield strength;

(4) The FSP post-treatment of SLM parts leads to the typical ”M” shape residual stress distribution, the stress level being higher than that in the as built SLM samples without preheating. The tensile residual stress level is however only 53% of the yield strength of the FSPed sample;

(5) The preheating of build platform appears to present a beneficial effect on porosity mitigation in the SLM process.

The results and conclusions reported here may be used to validate numerical simulations in the additive manufacturing community. In particular, the present work would help to promote our understanding of the decisive effect of the preheating on microstructure, residual stress, porosity, as well as the corresponding mechanical strength, ductility and fatigue resistance.

Acknowledgements

This research work has been supported from January 2019 by the WALInnov LongLifeAM project, Convention n°1810016, funded by the Service public de Wallonie Économie Emploi Recherche (SPW-EER). A. Simar acknowledges the financial support of the European Research Council (ERC) for the Starting Grant ALUFIX project (grant agreement n°716678). J. G. Santos Macías acknowledges the support of the Fonds de la recherche scientifique - FNRS (FRIA grant), Belgium. The authors acknowledge the technical support of the LEMSC team, in particular A. Bertholet from UCLouvain. The authors also acknowledge the support of J. Adrien and E. Maire from INSA Lyon for the X-ray tomography porosity measurements. Sirris and Any-Shape are acknowledged for material supply.

References

[1] E. O. Olakanmi, R. F. Cochrane, K. W. Dalgarno, A review on selective laser sintering/melting (SLS/SLM) of aluminium alloy powders: Processing, microstructure, and properties, Progress in Materials Science 74 (2015) 401–477. doi:10.1016/j.pmatsci.2015.03.002.

[2] T. DebRoy, H. L. Wei, J. S. Zuback, T. Mukherjee, J. W. Elmer, J. O. Milewski, A. M. Beese, A. Wilson-Heid, A. De, W. Zhang, Additive manufacturing of metallic components – Process, structure and properties, Progress in Materials Science 92 (2018) 112–224. doi:10.1016/j.pmatsci.2017.10.001.

[3] J. Zhang, B. Song, Q. Wei, D. Bourell, Y. Shi, A review of selective laser melting of aluminum alloys: Processing, microstructure, property and developing trends, Journal of Materials Science & Technology 35 (2019) 270–284. doi:10.1016/j.jmst.2018.09.004.

[4] J. L. Bartlett, X. Li, An overview of residual stresses in metal powder bed fusion, Addtive Manufacturing 27 (2019) 131–149. doi:10.1016/j.addma.2019.02.020.

[5] D. Deng, J. Moverare, R. L. Peng, H. Söderbergb, Microstructure and anisotropic mechanical properties of ebm manufactured inconel 718 and effects of post heat treatments, Materials Science and Engineering A 693 (2017) 151–163. doi:10.1016/j.msea.2017.03.085.

[6] C. Huang, X. Yan, L. Zhao, M. Liu, W. Ma, W. Wang, J. Soete, A. Simar, Ductilization of selective laser melted Ti6Al4V alloy by friction stir processing, Materials Science and Engineeing A 755 (2019) 85–96. doi:10.1016/j.msea.2019.03.133.

[7] N. Hrabe, T. Gnäupel-Herold, T. Quinn, Fatigue properties of a titanium alloy (Ti-6Al-4V) fabricated via electron beam melting (EBM): Effects of internal defects and residual stress, International Journal of Fatigue 94 (2017) 202–210. doi:10.1016/j.ijfatigue.2016.04.022.

[8] J. G. Santos Macías, C. Elangeswaran, L. Zhao, B. Van Hooreweder, J. Adrien, E. Maire, J. Y. Buffière, W. Ludwig, P. J. Jacques, A. Simar, Ductilisation and fatigue life enhancement of selective laser melted AlSi10Mg by friction stir processing, Scripta Materialia 170 (2019) 124–128. doi:10.1016/j.scriptamat.2019.05.044.

[9] G. Strano, L. Hao, R. M. Everson, K. E. Evans, Surface roughness analysis, modelling and prediction in selective laser melting, Journal of Materials Processing Technology 213 (2013) 589–597. doi:10.1016/j.jmatprotec.2012.11.011.

[10] D. Greitemeier, C. D. Donne, F. Syassen, J. Eufinger, T. Melz, Effect of surface roughness on fatigue performance of additive manufactured Ti-6Al-4V, Materials Science and Technology 32 (2016) 629–634. doi:10.1179/1743284715Y.0000000053.

[11] P. Mercelis, J. P. Kruth, Residual stresses in selective laser sintering and selective laser melting, Rapid Prototyping Journal 12 (5) (2006) 254–265. doi:10.1108/13552540610707013.

[12] P. Edwards, M. Ramulu, Fatigue performance evaluation of selective laser melted Ti-6Al-4V, Materials Science and Engineering A 598 (2014) 327–337. doi:10.1016/j.msea.2014.01.041.

[13] V. Cain, L. Thijs, J. V. Humbeeck, B. V. Hooreweder, R. Knutsen, Crack propagation and fracture toughness of Ti6Al4V alloy produced by selective laser melting, Additive Manufacturing 5 (2015) 68–76. doi:10.1016/j.addma.2014.12.006.

[14] B. Vrancken, V. Cain, R. Knutsen, J. V. Humbeeck, Residual stress via the contour method in compact tension specimens produced via selective laser melting, Scripta Materialia 87 (2014) 29–32. doi:10.1016/j.scriptamat.2014.05.016.

[15] C. R. Knowles, T. H. Becker, R. B. Tait, Residual stress measurements and structural integrity implications for selective laser melted Ti-6Al-4V, The South African Journal of Industrial Engineering 23 (3) (2012) 119.

575 doi:10.7166/23-3-515.

576 [16] X. Zhao, X. Lin, L. Xue, W. Huang, The effect of hot isostatic pressing on crack healing, microstructure,
577 mechanical properties of Rene88DT superalloy prepared by laser solid forming, Materials Science and En-
578 gineering A 504 (2009) 129–134. doi:10.1016/j.msea.2008.12.024.

579 [17] M. Matsumoto, M. Shiomi, K. Osakada, F. Abe, Finite element analysis of single layer forming on metallic
580 powder bed in rapid prototyping by selective laser processing, International Journal of Machine Tools and
581 Manufacture 42 (2002) 61–67. doi:10.1016/S0890-6955(01)00093-1.

582 [18] C. H. Fu, Y. B. Guo, Three-dimensional temperature gradient mechanism in selective laser melting of Ti-
583 6Al-4V, Journal of Manufacturing Science and Engineering 136 (2014) 061004. doi:10.1115/1.4028539.

584 [19] L. Parry, I. A. Ashcroft, R. D. Wildman, Understanding the effect of laser scan strategy on residual stress
585 in selective laser melting through thermo-mechanical simulation, Additive Manufacturing 12 (2016) 1–15.
586 doi:10.1016/j.addma.2016.05.014.

587 [20] T. Mukherjee, W. Zhang, T. DebRoy, An improved prediction of residual stresses and dis-
588 tortion in additive manufacturing, Computational Materials Science 126 (2017) 360–372.
589 doi:10.1016/j.commatsci.2016.10.003.

590 [21] M. Galati, L. Iuliano, A literature review of powder-based electron beam melting focusing on numerical
591 simulations, Additive Manufacturing 19 (2018) 1–20. doi:10.1016/j.addma.2017.11.001.

592 [22] M. Galati, L. Iuliano, S. Salmi, E. Atzeni, Modelling energy source and powder properties for the develop-
593 ment of a thermal FE model of the EBM additive manufacturing process, Additive Manufacturing 14 (2017)
594 49–59. doi:10.1016/j.addma.2017.01.001.

595 [23] M. Galati, A. Snis, L. Iuliano, Powder bed properties modelling and 3D thermo-mechanical simulation
596 of the additive manufacturing Electron Beam Melting process, Additive Manufacturing 30 (2019) 100897.
597 doi:10.1016/j.addma.2019.100897.

598 [24] G. Vastola, G. Zhang, Q. X. Pei, Y. W. Zhang, Controlling of residual stress in additive man-
599 ufacturing of Ti6Al4V by finite element modeling, Additive Manufacturing 12 (2016) 231–239.
600 doi:10.1016/j.addma.2016.05.010.

601 [25] P. J. Withers, H. K. D. H. Bhadeshia, Residual stress. Part 1 – Measurement techniques, Materials Science
602 and Technology 17 (4) (2001) 355–365. doi:10.1179/026708301101509980.

603 [26] Y. Liu, Y. Yang, D. Wang, A study on the residual stress during selective laser melting (SLM) of metallic pow-
604 der, International Journal of Advanced Manufacturing Technology 87 (2016) 647–656. doi:10.1007/s00170-
605 016-8466-y.

606 [27] T. Simson, A. Emmel, A. Dwars, J. Böhm, Residual stress measurements on AISI 316L
607 samples manufactured by selective laser melting, Additive Manufacturing 17 (2017) 183–189.
608 doi:10.1016/j.addma.2017.07.007.

609 [28] P. Edwards, A. O'Conner, M. Ramulu, Electron beam additive manufacturing of titanium components:
610 Properties and performance, Journal of Manufacturing Science and Engineering 135 (2013) 061016.
611 doi:10.1115/1.4025773.

612 [29] I. Yadroitsev, I. Yadroitsava, Evaluation of residual stress in stainless steel 316L and Ti6Al4V
613 samples produced by selective laser melting, Virtual and Physical Prototyping 10 (2015) 67–76.

614 doi:10.1080/17452759.2015.1026045.
615 [30] L. Wang, X. Jiang, Y. Zhu, X. Zhu, J. Sun, B. Yan, An approach to predict the residual stress and distortion
616 during the selective laser melting of AlSi10Mg parts, The international Journal of Advanced Manufacturing
617 Technology 97 (2018) 3535–3546. doi:10.1007/s00170-018-2207-3.
618 [31] H. Ali, H. Ghadbeigi, K. Mumtaz, Effect of scanning strategies on residual stress and mechanical prop-
619 erties of Selective Laser Melted Ti6Al4V, Materials Science and Engineering A 712 (2018) 175–187.
620 doi:10.1016/j.msea.2017.11.103.
621 [32] C. Casavola, S. L. Campanelli, C. Pappalettere, Preliminary investigation on distribution of residual stress
622 generated by the selective laser melting process, The Journal of Strain Analysis for Engineering Design 44
623 (2009) 93–104. doi:10.1243/03093247JSA464.
624 [33] A. Salmi, E. Atzeni, L. Iuliano, M. Galati, Experimental Analysis of Residual Stresses on AlSi10Mg
625 Parts Produced by Means of Selective Laser Melting (SLM), Procedia CIRP 62 (2017) 458–463.
626 doi:10.1016/j.procir.2016.06.030.
627 [34] X. Wang, K. Chou, Residual stress in metal parts produced by powder-bed additive manufacturing processes,
628 in: Proceedings of the 26th International solid freeform fabrication symposium, 2015, pp. 1463–1474.
629 [35] J. L. Bartlett, B. P. Groom, J. Burdick, D. Henkel, X. Li, Revealing mechanisms of residual stress devel-
630 opment in additive manufacturing via digital image correlation, Additive Manufacturing 22 (2018) 1–12.
631 doi:10.1016/j.addma.2018.04.025.
632 [36] B. P. Croom, C. Bumgardner, X. Li, Unveiling residual stresses in air plasma spray coatings by digital image
633 correlation, Extreme Mechanics Letters 7 (2016) 126–135. doi:10.1016/j.eml.2016.02.013.
634 [37] C. Bumgardner, B. Croom, X. Li, High-temperature delamination mechanisms of thermal barrier coat-
635 ings: In-situ digital image correlation and finite element analyses, Acta Materialia 128 (2017) 54–63.
636 doi:10.1016/j.actamat.2017.01.061.
637 [38] Y. Zhan, C. Liu, J. Zhang, G. Mo, C. Liu, Measurement of residual stress in laser additive manufacturing TC4
638 titanium alloy with the laser ultrasonic technique, Materials Science and Engineering A 762 (2019) 138093.
639 doi:10.1016/j.msea.2019.138093.
640 [39] L. M. Sochalski-Kolbus, E. A. Payzant, P. A. Cornwell, T. R. Watkins, S. S. Babu, R. R. Dehoff, M. Lorenz,
641 O. Ovchinnikova, C. Duty, Comparison of Residual Stresses in Inconel 718 Simple Parts Made by Electron
642 Beam Melting and Direct Laser Metal Sintering, Metallurgical and Materials Transactions A 46 (3) (2015)
643 1419–1432. doi:10.1007/s11661-014-2722-2.
644 [40] K. An, L. Yuan, L. Dial, I. Spinelli, A. D. Stoica, Y. Gao, Neutron residual stress measurement and numerical
645 modeling in a curved thin-walled structure by laser powder bed fusion additive manufacturing, Materials &
646 Design 135 (2017) 122–132. doi:10.1016/J.MATDES.2017.09.018.
647 [41] H. J. Schindler, Experimental Determination of Crack Closure by the Cut Compliance Technique,
648 Advances in Fatigue Crack Closure Measurement and Analysis: Second Volume (1998) 175–
649 187doi:10.1520/STP15757S.
650 [42] M. B. Prime, Residual Stress Measurement by Successive Extension of a Slot: The Crack Compliance
651 Method, Applied Mechanics Reviews 52 (2) (1999) 75–96. doi:10.1115/1.3098926.
652 [43] M. B. Prime, Cross-sectional mapping of residual stresses by measuring the surface contour after a cut,

Journal of Engineering Materials and Technology 123 (2001) 162–168. doi:10.1115/1.1345526.

[44] B. Ahmad, S. O. van der Veen, M. E. Fitzpatrick, H. Guo, Residual stress evaluation in selective-laser-melting additively manufactured titanium (Ti-6Al-4V) and inconel 718 using the contour method and numerical simulation, Additive Manufacturing 22 (2018) 571–582. doi:10.1016/j.addma.2018.06.002.

[45] A. H. Maamoun, M. Elbestawi, G. K. Dosbaeva, S. C. Veldhuis, Thermal post-processing of AlSi10Mg parts produced by Selective Laser Melting using recycled powder, Additive Manufacturing 21 (2018) 234–247. doi:10.1016/j.addma.2018.03.014.

[46] EOS GmbH - Electro Optical Systems, Material Data Sheet for EOS Aluminium AlSi10Mg. München 2014.

[47] EOS GmbH - Electro Optical Systems, Material Data Sheet for Ti6Al4V for EOS M 290. München 2017.

[48] N. Takata, H. Kodaira, K. Sekizawa, A. Suzuki, M. Kobashi, Change in microstructure of selectively laser melted AlSi10Mg alloy with heat treatments, Materials Science and Engineering A 704 (2017) 218–228. doi:10.1016/j.msea.2017.08.029.

[49] I. Rosenthal, R. Shneck, A. Stern, Heat treatment effect on the mechanical properties and fracture mechanism in AlSi10Mg fabricated by additive manufacturing selective laser melting process, Materials Science and Engineering A 729 (2018) 310–322. doi:10.1016/j.msea.2018.05.074.

[50] A. H. Maamoun, S. C. Veldhuis, M. Elbestawi, Friction stir processing of AlSi10Mg parts produced by selective laser melting, Journal of Materials Processing Technology 263 (2019) 308–320. doi:10.1016/j.jmatprotec.2018.08.030.

[51] L. Zhao, J. G. Santos Macías, L. Ding, H. Idrissi, A. Simar, Damage mechanisms in selective laser melted AlSi10Mg under as built and different post-treatment conditions, Materials Science and Engineering A 764 (2019) 138210. doi:10.1016/j.msea.2019.138210.

[52] Z. L. Du, M. J. Tan, J. F. Guo, J. Wei, C. K. Chua, Dispersion of CNTs in selective laser melting printed AlSi10Mg composites via friction stir processing, Materials Science Forum 879 (2016) 1915–1920. doi:10.4028/www.scientific.net/MSF.879.1915.

[53] A. Hussein, L. Hao, C. Yan, R. Everson, Finite element simulation of the temperature and stress fields in single layers built without-support in selective laser melting, Materials & Design 52 (2013) 638–647. doi:10.1016/j.matdes.2013.05.070.

[54] Y. Li, K. Zhou, P. Tan, S. B. Tor, C. K. Chua, K. F. Leong, Modeling temperature and residual stress fields in selective laser melting, International Journal of Mechanical Sciences 136 (2018) 24–35. doi:10.1016/j.ijmecsci.2017.12.001.

[55] H. J. Schindler, W. Cheng, I. Finnie, Experimental Determination of Stress Intensity Factors Due to Residual Stresses, Experimental Mechanics 37 (3) (1997) 272–277. doi:10.1007/BF02317418.

[56] H. F. Bückner, A novel principle for computation of stress intensity factors, Zeitschrift für Angewandte Mathematik und Mechanik 50 (1970) 529–546.

[57] X. R. Wu, D. H. Tong, X. C. Zhao, W. Xu, Review and evaluation of weight functions and stress intensity factors for edge-cracked finite-width plate, Engineering Fracture Mechanics 195 (2018) 200–221. doi:10.1016/j.engfracmech.2018.04.001.

[58] X. R. Wu, A. J. Carlsson, Weight functions and stress intensity factor solutions, Pergamon Press, 1991.

[59] R. L. Ribeiro, M. R. Hill, A benchmark fracture mechanics solution for a two-dimensional eigenstrain prob-

lem considering residual stress, the stress intensity factor, and superposition, Engineering Fracture Mechanics 163 (2016) 313–326. doi:10.1016/j.engfracmech.2016.06.007.

[60] H. Tada, P. C. Paris, G. R. Irwin, The Stress Analysis of Cracks Handbook, Third Edition, ASME, Three Park Avenue New York, NY 10016-5990, 2000. doi:10.1115/1.801535.

[61] C. de Formanoir, S. Michotte, O. Rigo, L. Germain, S. Godet, Electron beam melted Ti-6Al-4V: Microstructure, texture and mechanical behavior of the as-built and heat-treated material, Materials Science and Engineering A 652 (2016) 105–119. doi:10.1016/j.msea.2015.11.052.

[62] EOS GmbH - Electro Optical Systems, Material Data Sheet for AlSi10Mg processed at a build platform temperature of 200°C for EOS M 280. München 2013.

[63] W. Woo, H. Choo, D. W. Brown, Z. Feng, P. K. Liaw, Angular distortion and through-thickness residual stress distribution in the friction-stir processed 6061-T6 aluminum alloy, Materials Science and Engineering A 437 (2006) 64–69. doi:10.1016/j.msea.2006.04.066.

[64] H. Lombard, D. G. Hattingh, A. Steuwer, M. N. James, Effect of process parameters on the residual stresses in AA5083-H321 friction stir welds, Materials Science and Engineering A 501 (2009) 119–124. doi:10.1016/j.msea.2008.09.078.

[65] K. Deplus, A. Simar, W. V. Haver, B. de Meester, Residual stresses in aluminium alloy friction stir welds, The International Journal of Advanced Manufacturing Technology 56 (2011) 493–504. doi:10.1007/s00170-011-3210-0.

[66] J. P. Kruth, J. Deckers, E. Yasa, R. Wauthlé, Assessing and comparing influencing factors of residual stresses in selective laser melting using a novel analysis method, Proceedings of the Institution of Mechanical Engineers, Part B: Journal of Engineering Manufacture 226 (2012) 980–991. doi:10.1177/0954405412437085.

[67] X. Yan, S. Yin, C. Chen, C. Huang, R. Bolot, R. Lupoi, M. Kuang, W. Ma, C. Coddet, H. Liao, M. Liu, Effect of heat treatment on the phase transformation and mechanical properties of Ti6Al4V fabricated by selective laser melting, Journal of Alloys and Compounds 764 (2018) 1056–1071. doi:10.1016/j.jallcom.2018.06.076.

[68] D. Buchbinder, W. Meiners, N. Pirch, K. Wissenbach, J. Scharge, Investigation on reducing distortion by preheating during manufacture of aluminum components using selective laser melting, Journal of Laser Applications 26 (2014) 012004. doi:10.2351/1.4828755.

[69] X. Zhao, S. Li, M. Zhang, Y. Liu, T. B. Sercombe, S. Wang, Y. Hao, R. Yang, L. E. Murr, Comparison of the microstructures and mechanical properties of Ti–6Al–4V fabricated by selective laser melting and electron beam melting, Materials & Design 95 (2016) 21–31. doi:10.1016/j.matdes.2015.12.135.

[70] A. Hadadzadeh, C. Baxter, B. S. Amirkhiz, M. Mohammadi, Strengthening mechanisms in direct metal laser sintered AlSi10Mg: Comparison between virgin and recycled powders, Additive Manufacturing 23 (2018) 108–120. doi:10.1016/j.addma.2018.07.014.

[71] T. Maconachie, M. Leary, J. Zhang, A. Medvedev, A. Sarker, D. Ruan, G. Lu, O. Faruque, M. Brandt, Effect of build orientation on the quasi-static and dynamic response of SLM AlSi10Mg, Materials science and Engineering A 788 (2020) 139445. doi:10.1016/j.msea.2020.139445.

[72] S. Tammas-Williams, P. J. Withers, I. Todd, P. B. Prangnell, Porosity regrowth during heat treatment of hot isostatically pressed additively manufactured titanium components, Scripta Materialia 122 (2016) 72–76. doi:10.1016/j.scriptamat.2016.05.002.

[73] K. V. Yang, P. Rometsch, T. Jarvis, J. Rao, S. Cao, C. Davies, X. Wu, Porosity formation mechanisms and fatigue response in Al-Si-Mg alloys made by selective laser melting, Materials Science and Engineering A 712 (2018) 166–174. doi:10.1016/j.msea.2017.11.078.

[74] Q. Guo, C. Zhao, L. I. Escano, Z. Young, L. Xiong, K. Fezzaa, W. Everhart, B. Brown, T. Sun, L. Chen, Transient dynamics of powder spattering in laser powder bed fusion additive manufacturing process revealed by in-situ high-speed high-energy x-ray imaging, Acta Materialia 151 (2018) 169–180. doi:10.1016/j.actamat.2018.03.036.

[75] S. A. Khairallah, A. A. Martin, J. R. I. Lee, G. Guss, N. P. Calta, J. A. Hammons, M. H. Nielsen, K. Chaput, E. Schwalbach, M. N. Shah, M. G. Chapman, T. M. Willey, A. M. Rubenchik, A. T. Anderson, Y. M. Wang, M. J. Matthews, W. E. King, Controlling interdependent meso-nanosecond dynamics and defect generation in metal 3D printing, Science 368 (2020) 660–665. doi:10.1126/science.aay7830.

[76] J. M. Bartlett, F. M. Heim, Y. V. Murty, X. Li, In situ defect detection in selective laser melting via full-field infrared thermography, Additive Manufacturing 24 (2018) 595–605. doi:10.1016/j.addma.2018.10.045.

[77] O. Holzmond, X. Li, In situ real time defect detection of 3D printed parts, Additive Manufacturing 17 (2017) 135–142. doi:10.1016/j.addma.2017.08.003.

[78] R. S. Mishra, Z. Y. Ma, Friction stir welding and processing, Materials Science and Engineering: R: Reports 50 (2005) 1–78. doi:10.1016/j.mser.2005.07.001.